

## Article

# U–Pb Dating of Fibrous Dolomite in the Hydrothermal Dolostone of the Dengying Formation, Central Sichuan Basin, and Its Response to Supercontinent Breakup

Jiang Zheng <sup>1,\*</sup>, Long Wen <sup>2</sup>, Yuhui Ge <sup>1</sup>, Gang Zhou <sup>2</sup>, Ya Zhang <sup>2</sup>, Wei Yan <sup>2</sup>, Huan Jiang <sup>1</sup>, Zili Zhang <sup>2</sup> and Aihua Xi <sup>1,\*</sup>

<sup>1</sup> School of Geoscience and Technology, Southwest Petroleum University, Chengdu 610500, China; geyuhui@swpu.edu.cn (Y.G.); 202111000024@stu.swpu.edu.cn (H.J.)

<sup>2</sup> Research Institute of Petroleum Exploration and Development, PetroChina Southwest Oil & Gas Field Company, Chengdu 610041, China; wenlong@petrochina.com.cn (L.W.); zhougang29@petrochina.com.cn (G.Z.); zhangya08@petrochina.com.cn (Y.Z.); yanwei-tlm123@petrochina.com.cn (W.Y.); zzl\_kyy@petrochina.com.cn (Z.Z.)

\* Correspondence: 202011000016@stu.swpu.edu.cn (J.Z.); xiaihua@swpu.edu.cn (A.X.)

**Abstract:** Super-deep drilling in the central Sichuan Basin encountered volcanic rocks of the Suxiong Formation, which are overlain by multiple hydrothermal alterations within the upper section of the Ediacaran Dengying Formation. This provides an excellent research opportunity to understand the pre-Cambrian hydrothermal activity and geological evolution of the western margin of the Yangtze Craton. Observations revealed the development of a series of hydrothermal dolomite aggregates characterized by the presence of brown sphalerite within fractures and pores of the carbonate rock. Microscopically, the dolomite exhibited fibrous columnar crystallization, forming radial bands with a gradual decrease in crystallization intensity from the center to the periphery. Cathodoluminescence analysis revealed the presence of approximately eight dolomite bands within the aggregate. U–Pb dating from the inner to outer bands yielded isotopic ages of  $781 \pm 12$  Ma for the second band,  $683 \pm 12$  Ma for the fifth,  $562 \pm 12$  Ma for the sixth, and  $545.4 \pm 6.9$  Ma for the seventh. The in situ rare earth element (REE) distribution patterns of the 781 and 683 Ma dolomite bands exhibited similarities. They both showed low total REE content ( $\Sigma$ REE), with significant fractionation between light and heavy REEs. Additionally, they exhibited negative anomalies in cerium (Ce) and europium (Eu), while heavy REEs were relatively enriched. The dolomite bands at 562 and 545 Ma also exhibited similar REE characteristics, with low  $\Sigma$ REE and weak fractionation between light and heavy REEs. They also displayed distinct negative anomalies in Ce and Eu, indicating similar distribution patterns. These findings suggested that formation of the banded hydrothermal dolostone occurred during different tectonic events, and the presence of heavy REE-enriched hydrothermal fluids suggested a deep-seated origin. This study has provided preliminary evidence that the Dengying Formation, previously considered to be of the Ediacaran age, has undergone multiple episodes of deep-seated fluid infiltration and alteration since the Mesoproterozoic Era. Importantly, these events coincide with the rifting of the Rodinia and Pannotia supercontinents, aligning with their respective timeframes. This finding raises questions regarding the stratigraphic division and correlation of the formations in the deeply buried core area of the basin.

**Keywords:** Dengying Formation; hydrothermal dolomite; laser ablation U–Pb dating; Sichuan Basin; Yangtze Craton



**Citation:** Zheng, J.; Wen, L.; Ge, Y.; Zhou, G.; Zhang, Y.; Yan, W.; Jiang, H.; Zhang, Z.; Xi, A. U–Pb Dating of Fibrous Dolomite in the Hydrothermal Dolostone of the Dengying Formation, Central Sichuan Basin, and Its Response to Supercontinent Breakup. *Minerals* **2023**, *13*, 1353. <https://doi.org/10.3390/min13101353>

Academic Editor: José Javier Alvaro

Received: 14 August 2023

Revised: 30 September 2023

Accepted: 16 October 2023

Published: 23 October 2023



**Copyright:** © 2023 by the authors. Licensee MDPI, Basel, Switzerland. This article is an open access article distributed under the terms and conditions of the Creative Commons Attribution (CC BY) license (<https://creativecommons.org/licenses/by/4.0/>).

## 1. Introduction

In recent years, numerous researchers have reported evidence of the involvement of the Yangtze Plate in the amalgamation and breakup of supercontinents such as Columbia, Rodinia, Gondwana, and Pangea. This evidence encompasses intense activity in terms of

tectonic, magmatic, and metamorphic events, as well as paleomagnetic data [1–7]. During the Early Neoproterozoic, volcano-sedimentary rock sequences such as the Suxiong and Xiaoxiangling Formations, which developed around the periphery of the Yangtze Craton, were products of continental rifting and marked the onset of the breakup of the Rodinia supercontinent [8]. Subsequently, following the breakup of the Pangea supercontinent, the global cycle of plate tectonics transitioned into the modern land–ocean evolution system. Along the western margin of the Yangtze Craton, a series of continuous collisions between multiple blocks occurred. The response of plate activities, including contact, collision, and orogenesis, was revealed within the Sanjiang Tectonic Belt based on abundant magmatic rocks, hydrothermal alterations, and ore-forming ages [1,9–13]. On a broader geological scale, the fragmentation of supercontinents, driven by dynamic forces originating deep within the Earth, particularly within the asthenosphere, inevitably mobilized and uplifted deep-seated materials. This phenomenon initiated interactions between the deep-seated materials and the solid lithosphere, constituting a crucial pathway for the exchange of material between the crust and mantle throughout the prolonged evolutionary process of the Earth [14,15]. Indeed, this thermal effect has been observed to extend to the regions of Sichuan, Yunnan, Guizhou, and the Qinghai–Tibet Plateau. Hydrothermal lead–zinc mineralization within the dolostone of the Dengying Formation in the Sichuan–Yunnan–Guizhou region serves as evidence of fluid activity triggered by thermal events [16–18].

A previous study of deep carbonate rock reservoirs in the Sichuan Basin reported that hydrothermal dolostone, which serves as high-quality reservoir rock, developed around extensional rifts or aulacogens and exhibits distinct spatial and temporal associations with extensional fault structures [19]. Observations of core samples from the Dengying Formation in Well Pengtan-1 in the central Penglai area revealed that the high-quality reservoir intervals of dolostone have undergone multiple episodes of dissolution and filling by hydrothermal fluids. This has resulted in the development of fibrous and granular dolomite cementation as well as residual pore spaces and filled pores, including the widely recognized grape- and fringe-like structures frequently discussed in the petroleum industry. To examine the relationship between hydrothermal dissolution episodes, tectonic activity, and regional thermal events, samples were taken from the core section of Well Pengtan-1, which contains quartz-bearing hydrothermal dolomite with multiple grape- and fringe-like structures. Conducting U–Pb dating of the hydrothermal dolostone and analyzing rare earth and trace elements *in situ* within the minerals associated the different dolomite zones with different hydrothermal fluid properties, thus providing precise insights into their responses. These findings offer evidence for multiple episodes of hydrothermal superposition and alteration in the Dengying Formation, as well as the potential existence of older geological information in the region. Furthermore, by incorporating regional tectonic evolution data, these findings shed light on the constraints imposed by tectonic–hydrothermal interactions on the mechanisms of reservoir formation.

## 2. Geological Background

The northern margin of the Yangtze Craton is characterized by the Qinling–Dabie–Sulu orogenic belt, while the northwestern margin is associated with the Longmenshan Fault. The southwestern margin is marked by the Ailao Shan–Red River Fault, and the southeastern margin is defined by the Jiangnan orogenic belt. These margins are adjacent to the North China Craton, the Songpan–Ganzi terrane, the Indochina Block, and the Huaxia Block, respectively [20,21] (Figure 1). Above the Jinning–Sibao unconformity surface, the Yangtze Craton is characterized by the development of Late Qingbaikou, Nanhua, and Ediacaran formations during the middle–late Neoproterozoic [22]. The stratigraphic profile of the northern margin of the Yangtze Craton reveals the presence of several formations. The late stage of the Qingbaikou formations is represented by the Huashan, Bikou, and Wudang Groups. The Nanhua formations are characterized by the Liantuo, Gucheng, Datangpo, and Nantuo Formations. The Ediacaran formations include the Doushantuo and Dengying Formations [23]. The Doushantuo Formation (ca. 635–551 Ma [24]) primarily

consists of sandstone and mudstone, while the Dengying Formation (ca. 551–541 Ma) is predominantly composed of clastic rock and dolostone [25,26].

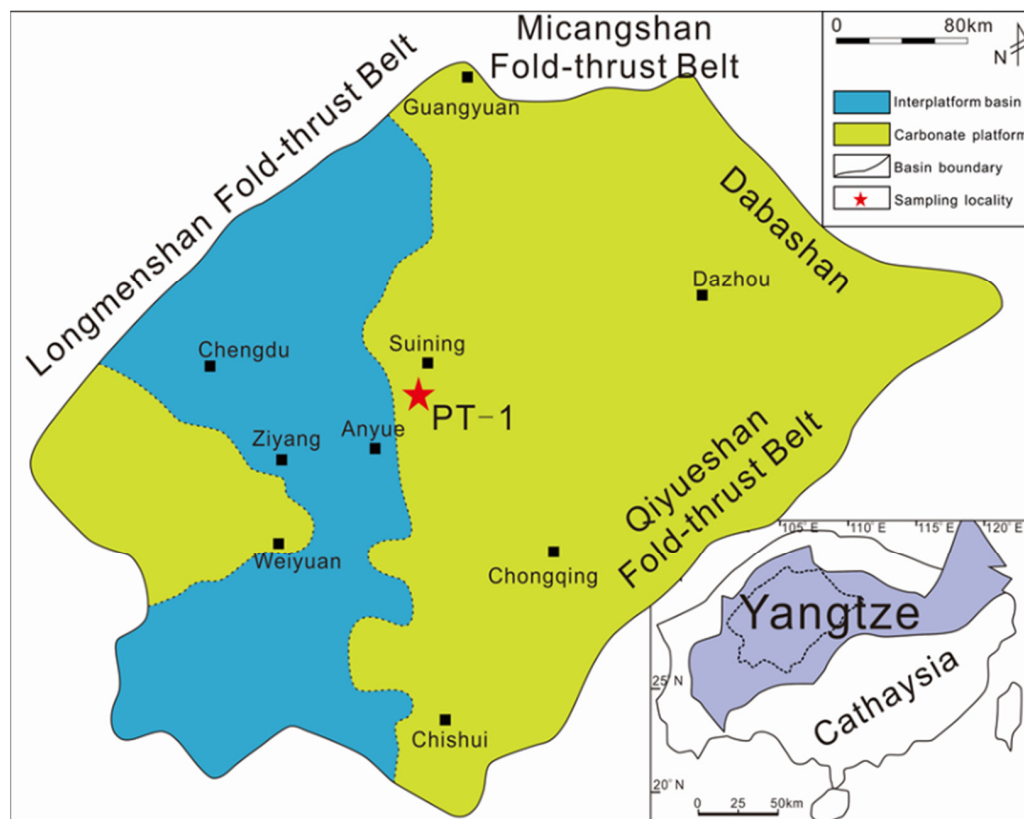


**Figure 1.** Paleogeographic map of the Yangtze Block during the late Ediacaran [27].

The Sichuan Basin, situated as a secondary tectonic unit on the Yangtze platform, evolved on the foundation of the Upper Yangtze Craton. It formed as a rhomboid-shaped polycyclic superimposed basin under the control of intersecting northeast and northwest deep faults [28]. After the conclusion of the Nanhua Period glaciation, the global climate warmed, and sea levels rose. As a result, the basin began to experience sedimentation of the Douxiantuo Formation, which is primarily composed of black shale, carbonate rock, siliceous rock, and phosphorite [29]. The Dengying Formation is a sedimentary sequence that developed following the deposition of the Doushantuo Formation [30]. It is primarily characterized by the accumulation of shallow-water carbonate platform deposits, indicating a marine-transgressive sedimentary sequence. The lower portion of the Dengying Formation shows conformable contact with the Doushantuo Formation, while the upper portion exhibits an unconformable contact with the Cambrian Maidiping Formation, indicating sedimentary hiatus. Based on lithological characteristics, the Dengying Formation can be further subdivided into four members [31]. The lithology of Deng-1 Member (member 1 of the Dengying Formation) exhibits distinct differences from the underlying strata, consisting predominantly of massive dolostone with minimal presence of grape- or fringe-like structures. The lowermost part of the Deng-1 Member exhibits a parallel unconformity contact with the underlying Doushantuo Formation, and a weathering crust is observed between them, as seen in the Nanjiang Yangba section and other locations. The lower part of Deng-2 Member is distinguished by the presence of abundant grape- and fringe-like structures, along with a significant occurrence of algal laminae. In the upper part, grape- and fringe-like structures are not well-developed; although algal laminae are still observable, they are less abundant compared to those in the lower part. Deng-3 Member represents a sequence of clastic rocks within the larger carbonate succession of the Dengying Formation in the Sichuan Basin and its surrounding regions. In the Shatan section of Nanjiang County,

bluish-gray mudstone containing volcanic ash is observed in the upper part of the Deng-3 Member. Deng-4 Member is characterized by blocky siliceous nodules and siliceous banded dolostone [32].

### 3. Materials and Methods

#### 3.1. Drilling Core Characteristics

In the interior of the Sichuan Basin, the Neoproterozoic strata are predominantly covered by Phanerozoic strata, with only a few wells encountering pre-Sinian strata. In the Weiyuan dome structure, several wells have been drilled through the sedimentary cover and reached the basement. However, no Nanhua Period strata have been observed or encountered. Instead, the lower part of the Dengying Formation of the Sinian Period directly overlays a granite basement with a zircon U–Pb age of  $794 \pm 11$  Ma [33]. In the northeastern part of the basin, Well Wutan-1 encountered sandstone rock of the Nanhua Period, specifically the Nantuo Formation. The sandstone rock exhibits poor sorting and rounding, similar to the lithology of the Nantuo Formation on the northern margin of the Yangtze Craton [34]. Multiple drilling wells within the Sichuan Basin have revealed distinct lithological characteristics in the high-quality dolostone reservoir rock of the Deng-2 Member. These rocks exhibit unique features, such as zebra-like, laminated, snowflake-like, conglomerate-like, and grape-like structures, distinguishing them from other layers within the Dengying Formation. Deng-3 Member is characterized by terrigenous clastic sandy and micritic dolostone, as well as dark gray to bluish-gray tuffaceous rock. Deng-4 Member primarily consists of shallow to deep-gray layered fine-grained dolostone and siliceous rock [35–38].

Well Pengtan-1 is located in the Penglai area in the central Sichuan Basin. It is a rare, ultra-deep well in the region that penetrated the strata of the Dengying Formation. In the pre-Cambrian section of Well Pengtan-1, the actual core length is 68.32 m, with depths ranging from 5726.18–5793.30 m for the Dengying Formation dolostone and from 6372.60–6376.00 m for the Suxiong Formation volcanic rock. Based on well logging and cuttings analysis, previous studies have determined the lithology of various intervals in Well Pengtan-1. The interval from 5628.5–5642 m is identified as Deng-3 Member, which consists of sandy dolostone with a notable abundance of quartz derived from terrigenous sources. The interval from 5642–6282 m corresponds to Deng-2 Member, mainly composed of fine-grained, sandy, and argillaceous dolostone. The interval from 6282–6350 m represents Deng-1 Member, consisting predominantly of argillaceous dolostone and micritic dolostone. The interval from 6350–6369 m is assigned to the Doushantuo Formation, characterized by sandy, argillaceous, and oolitic dolostone [39] (Figure 2).

In addition to micrite dolomite and clay minerals, the dolomite with “snowflake structure” also contains a large amount of idiomorphic columnar quartz, the content of which usually accounts for 5%–25% of the volume. It has a hexagonal columnar crystal shape in the cross section and an anisotropic distribution in the micrite dolomite matrix. When the local mud content is high, the rock transparency is reduced, and the lithology should be determined as (containing) quartz argillaceous dolomite. The traditional so-called “snowflake structure” shows that dolomite aggregates of medium-coarse-grained crystalline structure are semi-oriented along slender cracks, and the two ends are interspersed in the host argillitic limestone in a “fingertip” shape, showing the structural characteristics of late hydrothermal metasomatism-filling (Figure 3a,b). The “grape lace-like structure” can not only develop in the “snowflake structure” dolomite but can also exist in granular dolomite and grain dolomite. “Grape lace” is caused by partial dissolution cracks and dissolution hole edges of multi-phase fiber dolomite ring or “imbricate” superposition. It can be seen that the yellow-brown sphalerite and fiber dolomite symbiosis under the mirror, “grape lace” aggregate “fingertip”, interspersed in the powdery dolomite and quartz argillaceous dolomite. Occasionally, the sharp corners of the “fingertip” are cut by late hydrothermal dolomite (Figure 3c,d). Dolomite with “clumpy” or “brecciated” structure is strongly matched with hydrothermal transformation in terms of biological interval. In addition to the dissolution

pores and holes formed by the diffusion and transformation along the fractures in the later hydrothermal solution, it can also be seen that granular pyrite, coarse crystalline dolomite, crystalline cluster quartz, and even minerals fracture fillings such as potassium salt, stone salt, and apatite (Figure 3d). The crystalline dolomite is mainly composed of powdery and fine crystalline dolomite. The former usually has diffuse idiomorphic pyrite with a particle size of about 0.03~0.1 mm, which is considered to be the product of primary synsedimentation (Figure 3e). The content of mud in the medium-fine crystalline dolomite is low, and the sand shadow is occasionally seen. Some of the rocks recrystallized to form diamond-shaped idiomorphic dolomite with a particle size of about 0.05 mm, which has an obvious sense of particle boundary, which may represent the superposition transformation of late hydrothermal dolomitization. The argilly-rich “Psammitic phantom” may be the result of relative accumulation of argillaceous components after “recrystallization” of the original rock (Figure 3f).

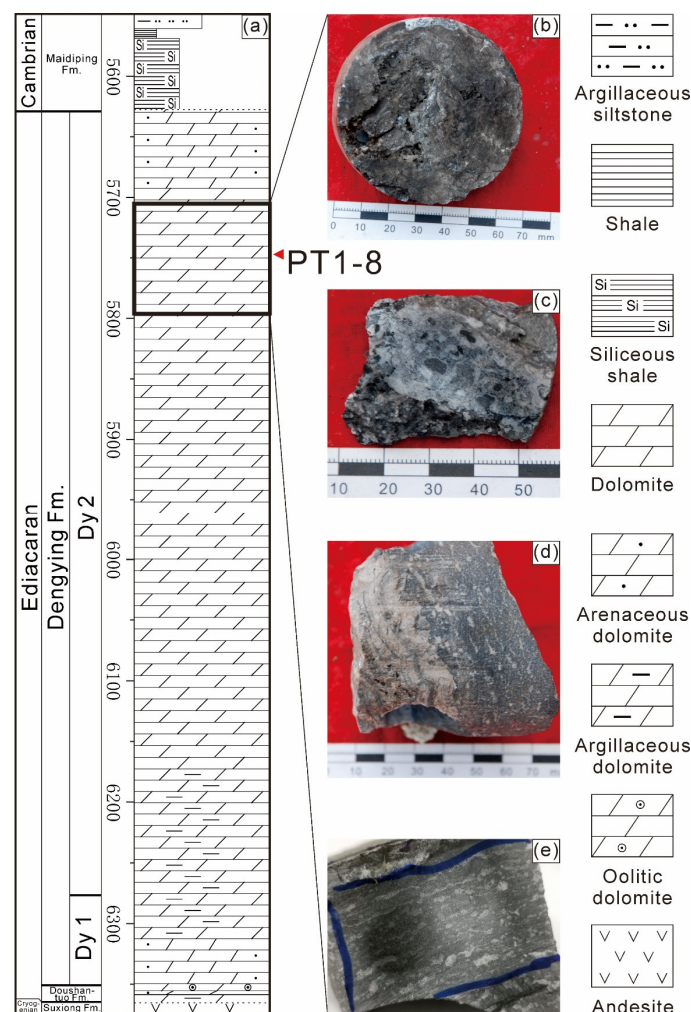


**Figure 2.** Comprehensive lithological column of the Dengying Formation in Well Pengtan-1. (a) Lithological column of the Dengying Formation in Well Pengtan-1; (b) Micrite dolostone; (c) Arenaceous dolostone; (d) Snowflake-like textured argillaceous dolostone; (e) Zebra-like textured dolostone.

### 3.2. Sample Selection

The studied sample, PT1-8, was collected from the Dengying Formation dolostone at a depth of 5748.80–5748.89 m in Well Pengtan-1. The sampling location is illustrated in Figure 2. The sample exhibited dark gray, snowflake-like (or nodular) white dolostone containing quartz and sphalerite. Microscopic examination revealed that the dolostone underwent multiple stages of dissolution and filling by hydrothermal fluids, resulting in

the formation of typical grape- and fringe-like structures. The grapevine edges consisted of multiple generations of fibrous white dolostone and sphalerite, as shown in Figures 3 and 4. Microscopic observation, in situ testing of rare earth elements (REEs), and U–Pb dating were conducted on the PT1-8 multi-stage hydrothermal dolomite. The cathodoluminescence and polarized light microscopic observations were conducted at the State Key Laboratory of Oil and Gas Reservoir Geology and Exploitation, Southwest Petroleum University (Chengdu, China). The preparation of samples for REE and U–Pb isotope analysis, as well as the analytical measurements, were carried out at Micro-Origin and Spectrum Laboratory (Sichuan Chuangyuan Weipu Analytical Technology Co., Ltd.).

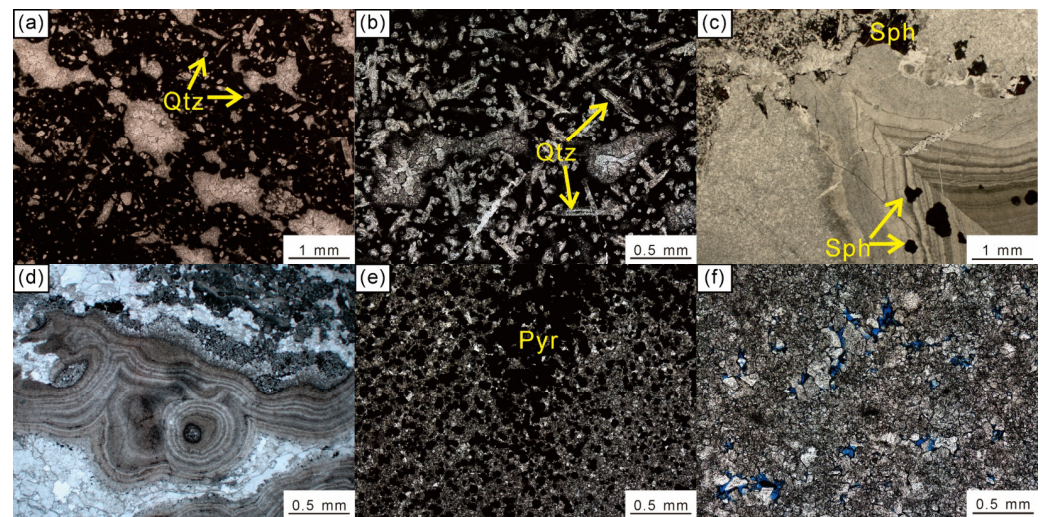


**Figure 3.** Lithological and dissolution-filling features of the core section in Well Pengtan-1. (a) The Dolomites exhibit pear-shaped diffusion-like fractures, which are filled with multi-stage fine and medium-crystalline dolomites; (b) The mudstone–dolostone contains abundant well-formed quartz crystals predominantly occurring as elongated prisms and hexagonal sections. Fibrous and granular dolomite (under cross-polarized light) fills the intergranular pores between the quartz grains; (c) Dissolution fissures and structural fractures developed within the snowflake-like textured argillaceous dolostone. Multiple generations of fibrous dolomite and brownish-yellow sphalerite can be observed within the dissolution fissures, and granular dolomite can be seen filling the remaining spaces (under plane-polarized light); (d) The micrite dolomite contains a significant quantity of dispersed pyrite, which is predominantly in a granular form with particle sizes ranging from approximately 0.03 to 0.1 mm; (e) Fine-grained dolomite exhibits minimal intergranular pore development, resulting in a compact texture; (f) The original fabric of mesocrystalline dolomite, which has been completely reformed by hydrothermal solution, is almost imperceptible, rendering the entire structure completely recrystallized into coarse dolomite. Qtz, quartz; Sph, sphalerite; Pyr, pyrite.

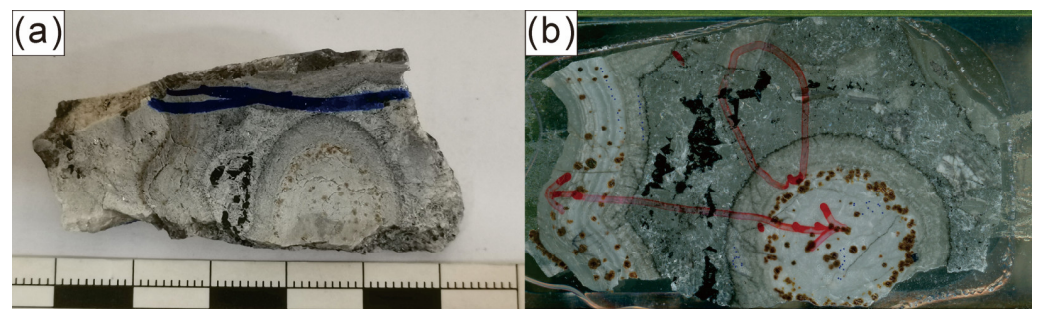


**Figure 4.** PT1-8 sample of Deng-2 Member in Well Pengtan-1. (a) The side view of the sample; (b) The top view of the sample).

### 3.3. Experimental Analysis

The instruments used for the CL examination were a polarizing microscope (DM2500P, Leica, Wetzlar, Germany) and CL spectroscope (CL8200MK5, CITL, Corby, UK).

The test of the trace element procedure is presented below: First, sample PT1-8 is selected under the microscope for the in situ analysis. Samples are made into relatively thick–thin sections, on which each laser ablation spot is specified via the polarizing and reflected-light microscopy to determine the oncolite positions (marked using a marking pen). Before testing, the thin sections are ultrasonically-treated with ultrapure water. The samples are then tested using the ICP-MS (Agilent 7800 ICP-MS, Agilent, Santa Clara, CA, USA), integrated with the in situ laser ablation device (COMPexPro lasers, Coherent, Longmont, CO, USA). A NIST 612 reference material spot is set for every five testing spots for drift correction. Before running tests, the calibration curve is built using a series of reference materials, including MACS-3, NIST 612, and NIST 610. The laser ablation of the LA-ICP-MS adopts the single-spot ablation mode, and the laser beam has a diameter of 44  $\mu\text{m}$ . The test is composed of the first 20 s blank sampling, then 45 s continuous ablation sampling, 20 s post-ablation purging of the sampling system, and finally, 85 s testing of a single spot. The collected data are processed offline using Iolite 3.6.

The testing process of laser ablation U–Pb dating involved the use of laser ablation inductively coupled plasma mass spectrometer (LA-ICP-MS) for in situ element analysis of the target minerals. Regions with a high  $\text{U}^{238}/\text{Pb}^{206}$  ratio and low  $\text{Pb}^{206}$  content were selected. For U–Pb isotope analysis, a quadrupole-based inductively coupled plasma mass spectrometer (iCap-RQ ICP-MS, Thermo Fisher Scientific, Waltham, MA, USA) equipped with a 43  $\mu\text{m}$  resolution laser ablation system was used. The laser beam had a diameter of 120  $\mu\text{m}$ , and the energy density was set at 2.5  $\text{J}/\text{cm}^2$  with an ablation frequency of 10 Hz. Helium gas with appropriate amounts of argon and nitrogen gas was introduced as the carrier gas. Each measurement point had a background acquisition time of 20 s, data collection time of 25 s, and sample cleaning time of 10 s. The reference standard NIST612, with  $^{43}\text{Ca}$  as an internal standard, was used to calibrate the trace element content of the samples. The standards NIST 614 and ARM-3 were used to correct for instrument sensitivity drift and  $^{207}\text{Pb}/^{206}\text{Pb}$  ratios. The standard AHX-1D (sample age  $238.2 \pm 1.3$  Ma) was primarily used to calibrate the  $^{238}\text{U}/^{206}\text{Pb}$  ratio. Iolite v3.4 software was employed for data processing, followed by the use of Isoplot 3.0 for age calculations and concordia diagram plotting.

## 4. Results

### 4.1. Characteristics of Multi-Stage Fibrous Dolomite Bands

Under polarized light microscopy and cathodoluminescence examination, the sample exhibited nine distinct generations of dolomite cement that developed from the matrix edge towards the center of the pores. They represent characteristic results of successive periods of hydrothermal cementation and filling at different stages (see Figure 5). The nine generations of dolomite aggregates in the sample, from the matrix edge towards the center of the pores, were as follows: ① Pale yellow radial dolomite with no cathodoluminescence; ② yellow-brown multiband fibrous dolomite with dark red cathodoluminescence coexisting with coarse-grained sphalerite during this period (see Figure 5); ③ and ④ pale yellow radial dolomite with no cathodoluminescence; ⑤ pale yellow radial dolomite with dark red cathodoluminescence coexisting with sphalerite during this period; ⑥ pale yellow-white rimmed acicular dolomite transitioning to dark red cathodoluminescence; ⑦ pale yellow-white acicular dolomite exhibiting brighter orange-red cathodoluminescence than that of the previous six generations; ⑧ transparent fine-grained dolomite with no cathodoluminescence; and ⑨ coarse-grained dolomite with bright orange-red cathodoluminescence.

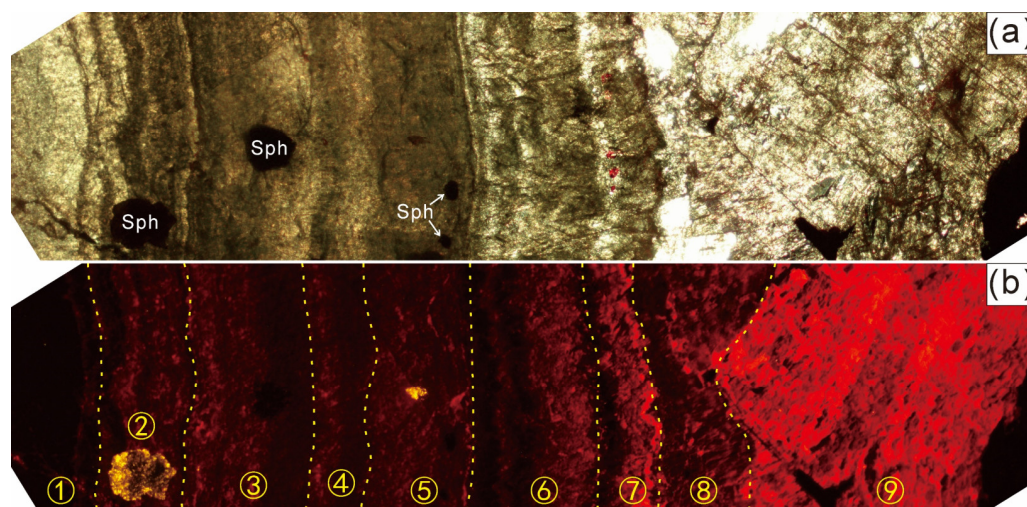


**Figure 5.** Optical characteristics of multi-stage fibrous dolomite with grape-like banding structures. (a) Microscope image of botryoidal dolomite merged by eight views, showing the nine generations of dolomite aggregates in the sample, from the matrix edge towards the center of the pores; (b) the emerged CL images of (a).

#### 4.2. U–Pb Isotopic Ages of Dolomite

##### 4.2.1. U–Pb Dating Results of the Core Part of the Grape-like Rim Dolomite

Isotope analysis began in the region shown in Figure 5, where the outer band ① of pale yellow radial dolomite was not sampled. Dating was conducted on the core part of the inner band ② of yellow-brown fibrous dolomite, yielding a U–Pb age of  $781 \pm 12$  Ma for 80 points (Figure 6e). This result indicated the extreme age of the formation of the grape-like rim dolomite, corresponding to the early stage of the Neoproterozoic Nanhua Period.

##### 4.2.2. Age Determination of the Fifth Outer Band of Pale Yellow Radial Dolomite

The U–Pb discordant age of 58 points in the fifth outer band (⑤) of pale yellow radial dolomite was  $683 \pm 12$  Ma (Figure 6f), indicating an Early Ediacaran age in the Neoproterozoic era.

##### 4.2.3. U–Pb Dating of the Needle-Shaped Dolomite in the Sixth Outer Band Was as Follows

In the sixth zone (⑥), the colors observed under polarized and reflected light microscopy were different from those in the previous zones. The dolomite crystals in this zone had higher transparency and exhibited “plum-pit” and “spear-like” shapes. The U–Pb ages of 57 white marble samples were determined to be  $562 \pm 12$  Ma (Figure 6g), indicating a Late Ediacaran age. This age is consistent with the late stage of sedimentation in the Doushantuo Formation or the early stage of sedimentation in the Dengying Formation.

##### 4.2.4. U–Pb Dating of the Needle-Shaped Dolomite in the Seventh Outer Band Is as Follows

The needle-shaped dolomite in the seventh outer band (⑦) exhibited similar optical properties and mineral morphology to that in the sixth outer band (⑥). U–Pb dating analysis of 78 data points yielded an age of  $545.4 \pm 6.9$  Ma (Figure 6h), indicating the late Ediacaran period of the Neoproterozoic era. This age is consistent with the sedimentation timing of the Dengying Formation, suggesting a strong correlation. The fine-grained dolomite in the outermost bands (⑧ and ⑨) of the sample did not yield well-constrained isotopic ages due to low U/Pb ratios. However, based on their spatial occurrence, it is evident that these bright dolomite minerals are relatively younger and represent products of late-stage hydrothermal alteration and filling.

### 4.3. In-Situ Rare Earth Element Characteristics

To investigate the nature and sources of hydrothermal alteration during different periods, in situ trace element analysis was conducted on fibrous dolomite samples from the same horizons as the dated points (Table 1). The obtained results were normalized using the Sun and McDonough (1989) [40] method, which is based on the composition of spherical granules (Detailed data are shown in Table A1).

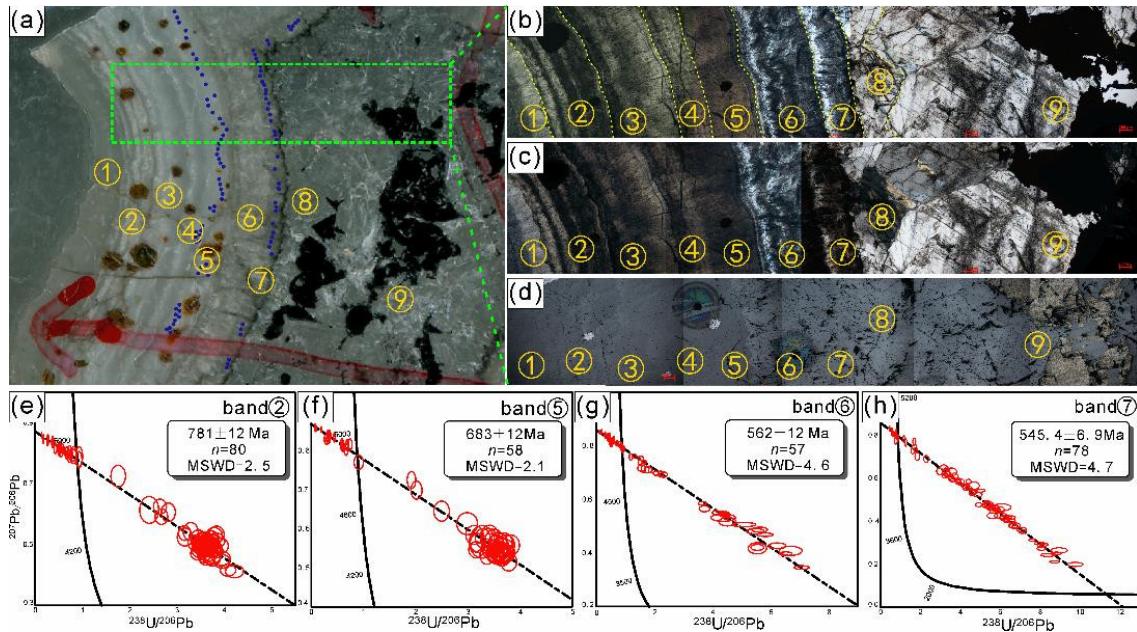


**Figure 6.** Distribution and results of multi-stage cementation dating points in cavity fillings in Well Pengtan-1 (PT1-8-1). (a) Photomicrograph of PT1-8-1 (blue dots in the figure are U-Pb test points); (b) Details of the (a); (c) Orthogonal polarization images of (b); (d) Reflective images of (b); (e) U-Pb dating results of dolomite in band ②; (f) U-Pb dating results of dolomite in band ⑤; (g) U-Pb dating results of dolomite in band ⑥; (h) U-Pb dating results of dolomite in band ⑦. Detailed dating data can be found in Table S1.

**Table 1.** Statistical characteristics of rare earth elements in different stages of dolomite minerals in Well Pengtan-1.

Mineral	Position in Sample	Average Characteristics of Rare Earth Elements ( $10^{-6}$ )					
		$\Sigma$ REE	LREE	HREE	L/H	$\delta$ Eu	$\delta$ Ce
Dol2	Second phase, brown-yellow needle-like dolomite	1.393	1.123	0.270	4.170	0.591	0.712
Dol5	Fifth phase, pale yellow needle-shaped dolomite	1.120	0.885	0.235	3.771	0.550	0.707
Dol6	Sixth phase, pale yellow foliated dolomite	5.126	3.866	1.260	3.112	0.629	0.268
Dol7	Seventh phase, pale yellow foliated dolomite	4.514	3.470	1.044	3.387	0.647	0.223

Dolx, dolomite period within the sample;  $\Sigma$ REE, total rare earth element; LREE, light rare earth element; HREE, heavy rare earth element; L/H, LREE to HREE ratio;  $\delta$ Ce =  $2 \times \text{Ce}_N / (\text{La}_N + \text{Pr}_N)$ ;  $\delta$ Eu =  $2 \times \text{Eu}_N / (\text{Sm}_N + \text{Gd}_N)$ .

- (1) Second phase dolomite (Dol2, 781 Ma) from the cores of the grape- and fringe-like structures had a total rare earth element content ( $\Sigma$ REE) ranging from  $(0.951\text{--}1.772) \times 10^{-6}$  with an average value of  $1.393 \times 10^{-6}$ . The ratio of light rare earth elements (LREEs) to heavy rare earth elements (HREEs) ranged from 3.915–4.527, indicating a generally right-skewed pattern of LREE enrichment (Figure 7a). The  $\delta$ Eu values ranged from

- 0.435–0.728, indicating a significant negative europium (Eu) anomaly. The  $\delta\text{Ce}$  values ranged from 0.694–0.741, indicating a pronounced negative cerium (Ce) anomaly.
- (2) The fifth phase of radial yellowish-white dolomite (Dol5) (683 Ma) showed relatively low  $\Sigma\text{REE}$  content, ranging from  $0.887 \times 10^{-6}$ – $1.279 \times 10^{-6}$  with an average of  $1.120 \times 10^{-6}$ . The LREE/HREE ratio ranged from 3.555–3.976, indicating a slightly enriched distribution pattern with a right-skewed trend in favor of LREE (Figure 7b). The  $\delta\text{Eu}$  values ranged from 0.440–0.678, and the  $\delta\text{Ce}$  values range from 0.677–0.741, exhibiting significant negative anomalies for Eu and Ce, respectively. The REE distribution of this type of dolomite was highly consistent with the morphology of the second period of dolomite in the core of the grape-like edge. It exhibited a low  $\Sigma\text{REE}$  content with no significant separation between LREEs and HREEs. The negative anomalies observed for Ce and Eu indicated that the dolomite contained relatively high concentrations of HREEs. This not only confirmed that they were products of the same major tectonic event, but also suggested that the hydrothermal fluids originated from deep-seated fluids in the mantle. These fluids may have been derived from the partial melting of the garnet clinopyroxenite source region, which is responsible for the enrichment of HREEs in the fluid.
  - (3) The in situ REE analysis of the needle-like dolomite in the sixth period (Dol6) (562 Ma) revealed a slightly greater  $\Sigma\text{REE}$  content compared to that in the earlier period. The  $\Sigma\text{REE}$  ranged from  $3.265 \times 10^{-6}$ – $7.937 \times 10^{-6}$  with an average of  $5.126 \times 10^{-6}$ . The LREE/HREE ratio ranged from 2.459–3.446, indicating a weak enrichment of LREEs in a right-skewed distribution pattern (Figure 7c). The  $\delta\text{Eu}$  values range from 0.602–0.658, while the  $\delta\text{Ce}$  values ranged from 0.164–0.360, both showing clear negative anomalies.
  - (4) The needle-like dolomite in the seventh period (Dol7) (545 Ma) exhibited the same characteristics as the dolomite in the sixth phase in terms of  $\Sigma\text{REE}$  content and distribution pattern (Figure 7d). It had a low  $\Sigma\text{REE}$  value with low significant fractionation between LREEs and HREEs. There were clear negative anomalies in Ce and Eu, confirming that they were products of the same major tectonic event, and the fluid also showed characteristics of a mantle source.

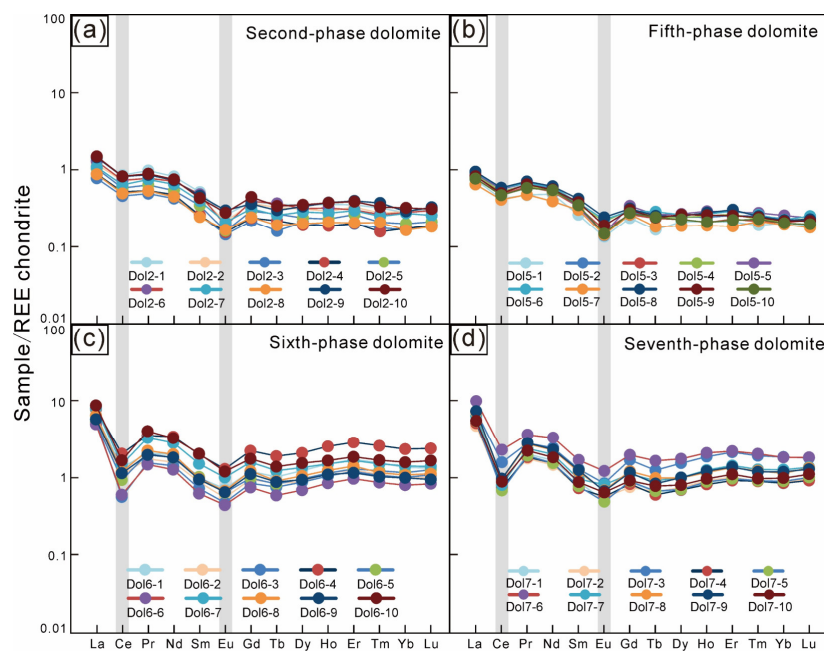


**Figure 7.** REE distribution patterns of multiple phases of dolomite in the Dengying Formation of Well Pengtan-1. (a) REE distribution pattern of yellow-brown banded fibrous dolomite in the second phase; (b) REE distribution pattern of pale yellow radial dolomite in the fifth phase; (c) REE distribution

pattern of pale yellow-white ring-shaped acicular dolomite in the sixth phase; (d) REE distribution pattern of pale yellow-white acicular dolomite in the seventh phase. REE, rare earth element. Dolx-x, number of sample test data point, shown in Table A1.

## 5. Discussion

### 5.1. Multi-Phase Dolomite Chronology

In recent years, LA-ICP-MS has gained popularity due to its high sensitivity and high spatial resolution. It has been widely applied in U–Pb dating of carbonate minerals, providing valuable insights into hydrothermal fluid activity, carbonate rock diagenesis, and the processes of oil and gas reservoir formation [41–43]. Shen et al. (2019) [44] dated different generations of dolomite cement in the dolostone of the Ediacaran Dengying Formation in the Sichuan Basin, China. The results provided insights into the sedimentary processes of the dolostone in the pore space, and the agreement between its age, tectonic movement, and thermal evolution history demonstrated the reliability and effectiveness of U–Pb dating of carbonate rocks. In the initial studies of carbonate mineral dating in the Ediacaran strata, previous researchers sampled and tested the Dengying Formation (551–541 Ma) from different regions. The research obtained age data from multiple phases, including 618–577 Ma, 556–543 Ma, 545–454 Ma, and 268–216 Ma (Figure 8). According to the stratigraphic classification of the Yangtze region for the Ediacaran strata, the sampling locations were all within the Dengying Formation (551–541 Ma), representing the late Ediacaran period. It is evident that some of the obtained data exceeded the age represented by the strata. However, it is unclear from the previous studies whether there were any anomalies in the ages reported, and no geological explanations were provided for these discrepancies.

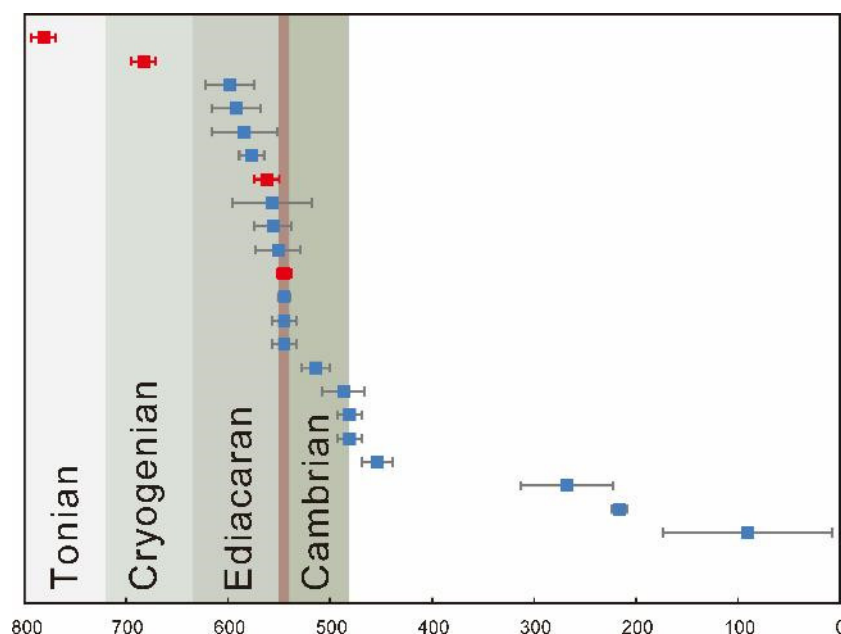


**Figure 8.** U–Pb age diagram of Ediacaran dolostone samples from the Sichuan Basin (thin lines represent error bars) (blue data from Shen et al., 2019 [44], red data from this study).

The multiple generations of dolomite cement tested in this study were derived from the fillings within fractures and cavities of the Dengying Formation dolomite. Based on their occurrence within the stratigraphic layers and their different colors observed under cathodoluminescence, these cements are likely slightly younger than the underlying bedrock and represent multiple phases of fluid infiltration and cementation. All measured points in the tested samples exceeded 50, exhibiting a wide range of variations in the  $^{238}\text{U}/^{206}\text{Pb}$  ratio. The ages obtained show small mean squared weighted deviations (MSWD) and low errors ( $2\sigma$ ), indicating tight clustering of the U–Pb age data points. This suggests that the uncertainties associated with the data are small (Figure 6). The present

study established U–Pb ages of 781 and 683 Ma for fibrous dolomite samples Dol2 and Dol5, respectively, which documented the timing of formation for early fibrous dolomite cement. These data challenge the defined sedimentation age limits (551–541 Ma) for the Ediacaran Dengying Formation [23,45]. Furthermore, previous studies have also reported multiple “beyond” ages within the Dengying Formation (Figure 8), suggesting that the sedimentation timing of the dolostone formation/strata considered part of the Dengying Formation in the Sichuan Basin may not be limited to the late Ediacaran period. The Dol6 acicular dolomite exhibited distinct colors under both polarized and reflected light (blue frame) with higher transparency compared to that of the previous samples. The crystallization age was approximately 562 Ma, which was consistent with the U–Pb age of fibrous dolomite cement in the grape-shaped dolomite from the Ebian Vanguard section in the Sichuan Basin reported by Lei et al. (2022) [46] as  $557 \pm 39$  Ma. This indicates a deposition time in the late Ediacaran period, corresponding to the end of the Doushantuo Formation sedimentation. The outermost ring of dolomite with a crystallization age of 545.4 Ma exhibited similar optical characteristics to the Dol6 acicular dolomite, as well as similar mineral morphology. This age is in conjunction with the sedimentation time of the Dengying Formation. The fine-grained dolomite in the outermost bands (⑧ and ⑨) of the sample did not yield well-constrained isotopic ages due to low U/Pb ratios. However, based on their spatial occurrence, it is evident that these bright dolomite minerals were relatively younger and represent products of late-stage hydrothermal alteration and filling.

### 5.2. Source of Hydrothermal Fluids

Lottermoser suggested that the relative abundance of REE in minerals precipitated from aqueous solutions is limitedly influenced by the crystallographic characteristics of the minerals themselves [47]. Instead, it primarily depends on the concentration of REEs in the fluid and the geochemical properties of the system. Undoubtedly, carbonate minerals formed by fluids other than the depositional fluids (such as hydrothermal carbonate minerals) inevitably bear the imprint of the associated fluids, serving as valuable clues for tracing their origins. Previous studies on the grape-like structures of the Ediacaran Dengying Formation in the Sichuan Basin proposed various genetic mechanisms, including depositional, quasi-syngenetic, epigenetic karst, and shallow burial diagenesis origins [48–51].

This study revealed the presence of coexisting brown sphalerite crystals in the first to fifth dolomite phases, indicating enrichment with lead, zinc, and sulfides in the ore-forming fluids. This suggested that the fluids were not related to seawater or freshwater during the depositional and shallow burial stages, but rather originated from typical low-temperature hydrothermal sources. The second and fifth periods of dolomite displayed a relatively low  $\Sigma$ REE with an average of  $1.25 \times 10^{-6}$  and weak fractionation. The REE distribution pattern exhibited a slight rightward inclination with evident negative anomalies of Eu and Ce, resembling the REE distribution pattern of the Doushantuo period volcanic-exhalative lead–zinc deposits in the later stage in the Yunnan–Guizhou area. This suggested that the early-stage hydrothermal fluids may have originated from deep hydrothermal sources and were linked to the multi-stage magmatic intrusions and lead–zinc mineralization events in response to the Rodinia continental rifting period on the western margin of the Yangtze Plate [52–54].

The fibrous dolomite crystals in the sixth and seventh phases were relatively clean and distinct from those in the first to fifth phases, as they lacked sphalerite mineralization. This indicated a change in the composition and source of the hydrothermal fluids during the late stage. REE analysis revealed that the fibrous dolomite cement from the second phase at 781 Ma had REE concentrations ranging from 0.951–1.772 ppm. In contrast, the cement from the latest stage at 545 Ma exhibited higher REE concentrations, ranging from 3.270–7.642 ppm (Figure 7). The variations in REE content among different phases of cementation indicated differences in the sources of fluids during different stages. These results indicated that the formation of mineralizing fluids at high temperatures may result in the characteristic negative anomalies of Ce and Eu. Although the samples exhibited

different REE patterns among various phases of dolomite cementation, they all displayed clear negative anomalies of Eu and Ce. This observation suggested a possible connection between the dolomitizing fluids and deep-seated high-temperature hydrothermal sources. Compared to the early-stage fibrous dolomite with U–Pb ages of 781 and 683 Ma, the 562 and 545 Ma dolomite samples exhibited an overall pattern of LREE enrichment characterized by a right-skewed curve in the distribution of REEs. The weighted  $\Sigma$ REE ( $W(\Sigma$ REE)) ranging from  $3.265 \times 10^{-6}$ – $7.937 \times 10^{-6}$  also indicated a higher enrichment of REEs. This similarity to the characteristics of REEs in the phosphatic jets associated with the Late Doushantuo to Cambrian slope deposits suggested a possible association of the late-stage fluids with mantle-derived fluids during the concurrent rift development processes [55,56].

5.3. Coupling between Regional Tectonic Evolution and Timing of Hydrothermal Activity

The Yangtze Plate has undergone multiple phases of tectonic rotation, while the interior of the Sichuan Basin on the western margin of the Yangtze Plate has exhibited repeated cycles of tectonic quiescence and activity [57–59]. During the active tectonic phases, the region exhibited frequent faulting, the development of special sedimentary structures, intrusive magmatism, and volcanic eruption activities. These phases were characterized by the widespread occurrence of mafic volcanic rocks (basalt) and intrusive rocks (diorite), as well as the extensive distribution of intermediate-acidic volcanic rocks and intrusive rocks, and the development of conglomerate and volcanoclastic deposits [60–62]. Of particular interest is the long-distance effect of hydrothermal fluids, where the tectonic-magmatic processes are likely to result in the ascent of deep-seated and even mantle-derived fluids along faults into shallow sedimentary formations such as the Ediacaran Dengying Formation, Cambrian Longwangmiao Formation, Permian Qixia–Maokou Formation, and even the Triassic Feixianguan–Jialinjiang–Leikoupo Formation. These carbonate rock units bear strong evidence of intense hydrothermal geological processes [63–66]. Scholars have indeed found a significant correlation between various types of mineralization systems, including their sources, hydrothermal activities, and mineralization ages, in the western margin of the Yangtze Plate through studies employing lithological analysis, rock geochemistry, isotope geochemistry, and zircon U–Pb dating (Figure 9). These studies have shed light on the connection between these mineralization processes and supercontinent rifting [67,68].

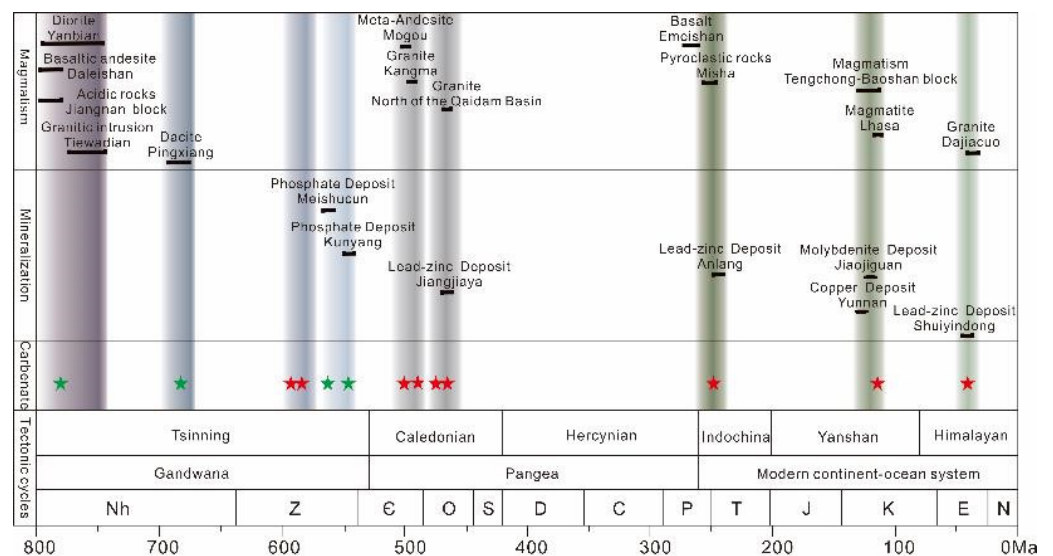


Figure 9. Coupling relationship between the regional tectonic rotation and magmatic mineralization (Green asterisks are the data in this article, red from [57–68]) (adapted from Ren et al., 2016 [69]).

The filling of fractures with hydrothermal minerals is considered a product of hydrothermal fluid events and serves as direct evidence of hydrothermal activity. In this study, the dating results of multi-phase fibrous dolomite in the grape-like edges of Well

Pengtan-1 show four age phases: the second phase, the fifth phase, the sixth phase, and the seventh phase, with ages of  $781 \pm 12$ ,  $683 \pm 12$ ,  $562 \pm 12$ , and  $545.4 \pm 6.9$  Ma, respectively (Figure 9). In comparison with the regional tectonic evolution, the age of 781 Ma roughly corresponds to the regional Chengjiang Movement and aligns with the initial rifting of the global Rodinia supercontinent [70,71]. The 683 Ma event occurred during the process of the Rodinia supercontinent breakup, during which volcanic eruptions and the deposition of the Liantuo Formation, Datangpo Formation volcanoclastic rocks, and terrigenous clastic rocks occurred in the South China Plate, forming a suite of sedimentary assemblages in an extensional environment [6,72–74]. The ages of 562 and 545 Ma are roughly associated with the sedimentation of the Dengying Formation. However, in terms of timing, they correspond to the initiation of the Pannotia supercontinent breakup. Particularly, the 545 Ma time point coincides with the onset of sedimentation of the Maidiping Formation, which includes phosphatic carbonate deposits. The Maidiping Formation, along with the overlying siliceous rock and carbonaceous black shale of the Qiongzhusi Formation and the carbonate rock of the Canglangpu and Longwangmiao Formations, constitutes a suite of marine rift-type sediments interpreted as indicative of volcanic eruptions [75].

Based on the extensive dating results of the Dengying Formation obtained by previous researchers, we correlated the data points with geological phases, tectonic evolution history, and magmatic ages that were active around the basin margins. The results revealed that hydrothermal calcite (dolomite) has isotopic ages at multiple phases, including 781, 683, 592, 584, 562, 546, 545, 546, 487, 474, 248, 115, 40, and 20 Ma [42]. The age range of 20–40 Ma corresponds to the timing of the Himalayan orogeny, while the age of 115 Ma may be associated with multiple stages of subduction events along the western margin of the Yangtze platform. The age of 248 Ma corresponds to the magmatic activity of the Emeishan large igneous province. The time range of 474–487 Ma may correspond to the early Ordovician mass extinction event. The ages of 562 and 545 Ma are consistent with the breakup of the Pannotia supercontinent. The phase of 592–584 Ma may be related to hydrothermal venting events during the sedimentation stage of the Doushantuo Formation. The ages of 781 and 683 Ma roughly coincide with the breakup of the Rodinia supercontinent.

## 6. Conclusions

- (1) The lithology of the core sections from the Dengying Formation in the Penglai area mainly consisted of snowy-textured mudstone with quartz crystals, hydrothermally altered clastic dolostone, and recrystallized grain dolostone. These rock types have undergone multiple episodes of hydrothermal dolostone alteration, lead–zinc mineralization, and silicification alteration.
- (2) By conducting U–Pb isotope dating on the grape-like multi-stage dolostone within the vugs of the dolostone, isotopic ages of  $781 \pm 12$  Ma (MSWD = 2.5),  $683 \pm 12$  Ma (MSWD = 2.1),  $562 \pm 12$  Ma (MSWD = 4.6), and  $545.4 \pm 6.9$  Ma (MSWD = 4.7) were obtained. Combined with the characteristics of altered minerals and REEs, these results indicated that the Dengying Formation dolostone underwent successive alteration and modification by deep-seated mantle-derived hydrothermal fluids during the mid-to-late Neoproterozoic.
- (3) The results of this research on thermal events in the western margin of the Yangtze Plate suggested that the four stages of alteration in the Dengying Formation dolostone may represent a distant response to the Rodinia and Pannotia supercontinent rifting events. Considering the geological age of the hydrothermal transformation of the drilling core samples, we are questioning whether the dolomite observed above the Suxiong Formation volcanic rock, which was revealed through drilling in the Sichuan Basin, actually belongs to the Ediacaran Dengying Formation.

**Supplementary Materials:** The following supporting information can be downloaded at: <https://www.mdpi.com/article/10.3390/min13101353/s1>, Table S1: The data of Uranium-lead isotope ratio.

**Author Contributions:** Conceptualization, J.Z. and A.X.; methodology, Y.G.; investigation, H.J.; resources, L.W., G.Z. and W.Y.; data curation, J.Z.; writing—original draft preparation, J.Z.; writing—review and editing, A.X.; supervision, Y.Z.; project administration, Z.Z.; funding acquisition, L.W., G.Z. and W.Y. All authors have read and agreed to the published version of the manuscript.

**Funding:** This research was funded by Research Institute of Petroleum Exploration and Development, PetroChina Southwest Oil & Gas Field Company grant No. XNSKTYJS2022-128.

**Data Availability Statement:** Data sharing is not applicable.

**Conflicts of Interest:** The authors declare no conflict of interest.

## Appendix A

**Table A1.** Lithogeochemical data of rare earth elements from dolomite minerals in Well Pengtan-1, expressed in parts per million.

	La	Ce	Pr	Nd	Sm	Eu	Gd	Tb	Dy	Ho	Er	Tm	Yb	Lu
Dol2	1.438	0.861	0.987	0.827	0.521	0.261	0.394	0.362	0.356	0.363	0.357	0.326	0.282	0.321
Dol2	1.186	0.730	0.784	0.736	0.450	0.217	0.374	0.329	0.316	0.297	0.332	0.280	0.293	0.294
Dol2	0.785	0.463	0.498	0.429	0.260	0.146	0.219	0.162	0.210	0.189	0.200	0.178	0.167	0.186
Dol2	0.894	0.525	0.542	0.484	0.262	0.156	0.239	0.221	0.194	0.189	0.204	0.159	0.175	0.192
Dol2	1.045	0.589	0.644	0.544	0.349	0.163	0.297	0.270	0.241	0.234	0.266	0.212	0.202	0.215
Dol2	1.300	0.743	0.782	0.719	0.489	0.193	0.398	0.371	0.321	0.324	0.308	0.268	0.284	0.303
Dol2	1.093	0.647	0.755	0.658	0.400	0.212	0.318	0.262	0.289	0.279	0.300	0.253	0.277	0.260
Dol2	0.881	0.501	0.539	0.453	0.247	0.169	0.245	0.193	0.202	0.211	0.207	0.209	0.166	0.185
Dol2	1.460	0.825	0.869	0.738	0.466	0.302	0.366	0.303	0.340	0.381	0.400	0.377	0.293	0.333
Dol2	1.498	0.831	0.896	0.760	0.437	0.282	0.449	0.344	0.357	0.380	0.394	0.334	0.326	0.315
Dol5	0.750	0.426	0.476	0.490	0.264	0.135	0.240	0.168	0.213	0.217	0.213	0.192	0.206	0.189
Dol5	0.835	0.527	0.649	0.584	0.358	0.141	0.283	0.262	0.248	0.245	0.259	0.255	0.235	0.213
Dol5	0.773	0.484	0.610	0.524	0.335	0.168	0.266	0.237	0.230	0.210	0.232	0.215	0.209	0.226
Dol5	0.875	0.526	0.637	0.533	0.360	0.216	0.306	0.249	0.246	0.256	0.270	0.230	0.219	0.238
Dol5	0.893	0.565	0.681	0.605	0.328	0.152	0.345	0.265	0.272	0.294	0.288	0.279	0.259	0.241
Dol5	0.927	0.591	0.670	0.607	0.379	0.229	0.298	0.289	0.265	0.271	0.297	0.264	0.228	0.254
Dol5	0.654	0.414	0.481	0.395	0.305	0.144	0.267	0.184	0.188	0.190	0.186	0.214	0.195	0.179
Dol5	0.950	0.591	0.712	0.617	0.425	0.245	0.318	0.257	0.255	0.282	0.307	0.254	0.225	0.231
Dol5	0.831	0.502	0.652	0.560	0.385	0.191	0.307	0.242	0.266	0.262	0.258	0.245	0.219	0.220
Dol5	0.776	0.474	0.586	0.551	0.352	0.149	0.277	0.245	0.229	0.211	0.225	0.232	0.205	0.198
Dol6	6.839	1.401	2.152	2.070	1.031	0.751	1.251	1.064	1.282	1.558	1.780	1.625	1.402	1.390
Dol6	5.596	1.126	1.814	1.653	0.918	0.574	0.990	0.886	0.916	1.210	1.293	1.152	1.016	1.056
Dol6	5.559	0.588	1.617	1.484	0.758	0.496	0.880	0.788	0.913	1.091	1.253	1.111	1.051	1.131
Dol6	8.135	2.128	3.690	3.568	2.076	1.347	2.320	1.974	2.173	2.645	2.992	2.701	2.441	2.496
Dol6	5.445	0.971	2.113	1.890	1.063	0.665	1.027	0.861	1.005	1.187	1.351	1.277	1.211	1.316
Dol6	5.161	0.628	1.537	1.320	0.650	0.463	0.778	0.616	0.719	0.884	1.006	0.903	0.834	0.868
Dol6	8.370	1.543	3.417	2.941	1.577	1.046	1.646	1.280	1.408	1.567	1.736	1.567	1.479	1.451
Dol6	6.700	1.236	2.320	2.095	1.012	0.703	1.269	0.943	1.099	1.287	1.468	1.209	1.125	1.173
Dol6	6.006	1.186	2.049	1.899	0.987	0.678	1.159	0.915	0.975	1.142	1.202	1.071	1.036	0.988
Dol6	9.090	1.740	4.207	3.405	2.131	1.248	1.834	1.446	1.610	1.732	1.938	1.750	1.648	1.730
Dol7	5.552	0.672	1.977	1.632	0.846	0.489	0.851	0.641	0.665	0.838	0.944	0.863	0.817	0.956
Dol7	4.628	0.726	1.728	1.418	0.716	0.533	0.730	0.638	0.723	0.883	0.987	0.866	0.855	0.924
Dol7	7.087	1.537	2.732	2.381	1.253	0.818	1.656	1.211	1.501	1.825	2.087	1.871	1.802	1.754
Dol7	5.061	0.726	1.795	1.497	0.706	0.549	0.803	0.582	0.672	0.791	0.891	0.874	0.825	0.892
Dol7	5.369	0.660	1.875	1.497	0.749	0.473	0.870	0.649	0.683	0.857	0.941	0.887	0.870	0.979
Dol7	9.817	2.245	3.566	3.256	1.649	1.183	1.917	1.611	1.709	2.046	2.157	1.986	1.786	1.781
Dol7	6.312	0.778	2.326	1.956	0.931	0.788	1.081	0.887	0.972	1.219	1.396	1.241	1.234	1.328
Dol7	7.049	0.926	2.671	2.225	1.157	0.662	1.174	0.961	0.960	1.134	1.312	1.190	1.105	1.298
Dol7	7.262	0.938	2.755	2.258	1.214	0.648	1.129	0.812	0.972	1.182	1.335	1.155	1.156	1.249
Dol7	5.419	0.861	2.179	1.784	0.849	0.623	0.886	0.755	0.778	0.937	1.073	0.944	0.958	1.076

## References

1. Yin, H.F.; Wu, S.B.; Du, Y.S.; Peng, Y.Q. South China defined as part of Tethyan archipelagic ocean system. *Earth Sci.—J. China Univ. Geosci.* **1999**, *24*, 1–12.
2. Huang, B.C.; Zhou, Y.X.; Zhu, R.X. Discussions on Phanerozoic evolution and formation of continental China, based on paleomagnetic studies. *Earth Sci. Front.* **2008**, *15*, 348–359.
3. Zhai, M.G. The main old lands in China and assembly of Chinese unified continent. *Sci. China Earth Sci.* **2013**, *56*, 1829–1852. [[CrossRef](#)]
4. Hu, P.Y.; Li, C.; Li, J.; Wang, M.; Xie, C.M.; Wu, Y.W. Zircon U-Pb-Hf isotopes and whole-rock geochemistry of gneissic granites from the Jitang complex in Leiwuqi area, eastern Tibet, China: Record of the closure of the Paleo-Tethys Ocean. *Tectonophysics* **2014**, *623*, 83–99. [[CrossRef](#)]
5. Li, S.H.; Deng, C.L.; Dong, W.; Sun, L.; Liu, S.Z.; Qin, H.F.; Yin, J.Y.; Ji, X.P.; Zhu, R.X. Magnetostratigraphy of the Xiaolongtan Formation bearing *Lufengpithecus keiyuanensis* in Yunnan, southwestern China: Constraint on the initiation time of the southern segment of the Xianshuihe-Xiaojiang fault. *Tectonophysics* **2015**, *655*, 213–226. [[CrossRef](#)]
6. Shu, L.S.; Wang, B.; Cawood, P.A.; Santosh, M.; Xu, Z.Q. Early Paleozoic and Early Mesozoic intraplate tectonic and magmatic events in the Cathaysia Block, South China. *Tectonics* **2015**, *34*, 1600–1621. [[CrossRef](#)]
7. Li, Y. The Neoproterozoic Magmatic Event at Mount Emei on the Western Margin of the Yangtze Block and Its Implications for the Disintegration of the Rodinia Supercontinent. Master's Thesis, Chengdu University of Technology, Chengdu, China, 2020.
8. Geng, Y.S.; Kuang, H.W.; Du, L.L.; Liu, Y.Q.; Zhao, T.P. On the Paleo-Mesoproterozoic boundary from the breakup event of the Columbia supercontinent. *Acta Petrol. Sin.* **2019**, *35*, 2299–2324. [[CrossRef](#)]
9. Pan, G.T.; Wang, L.Q.; Yin, F.G.; Zhu, D.C.; Geng, Q.R.; Liao, Z.L. Charm of landing of plate tectonics on the continent as viewed from the study of the archipelagic arc-basin system. *Geol. Bull. China* **2004**, *23*, 933–939.
10. Liu, S.W.; Yan, Q.R.; Li, Q.G.; Wang, Z.Q. Petrogenesis of granitoid rocks in the Kangding Complex, western margin of the Yangtze Craton and its tectonic significance. *Acta Petrol. Sin.* **2009**, *25*, 1883–1896.
11. Guo, L.S.; Liu, Y.L.; Liu, S.W.; Cawood, P.A.; Wang, Z.H.; Liu, H.F. Petrogenesis of Early to Middle Jurassic granitoid rocks from the Gangdese belt, Southern Tibet: Implications for early history of the Neo-Tethys. *Lithos* **2013**, *179*, 320–333. [[CrossRef](#)]
12. Qin, K.Z.; Zhai, M.G.; Li, G.M.; Zhao, J.X.; Zeng, Q.D.; Gao, J.; Xiao, W.J.; Li, J.L.; Sun, S. Links of collage orogenesis multiblocks and crust evolution to characteristic metallogenesis in China. *Acta Petrol. Sin.* **2017**, *33*, 305–325.
13. Li, W.C.; Jiang, X.J. The Cenozoic tectono-magmatism-mineralization effect of the intracontinental tectonic transformation system in the western margin of Yangtze Block. *Earth Sci. Front.* **2020**, *27*, 151–164. [[CrossRef](#)]
14. Wu, F.Y.; Xu, Y.G.; Zhu, R.X.; Zhang, G.W. Thinning and destruction of the cratonic lithosphere: A global perspective. *Sci. China Earth Sci.* **2014**, *57*, 2878–2890. [[CrossRef](#)]
15. Tang, D.J.; Shi, X.Y.; Liu, D.B.; Lin, Y.T.; Zhang, C.H.; Song, G.Y.; Wu, J.J. Terminal paleoproterozoic ooidal ironstone from north China: A sedimentary response to the initial breakup of columbia supercontinent. *Earth Sci.—J. China Univ. Geosci.* **2015**, *40*, 290–304. [[CrossRef](#)]
16. Wang, G.Z.; Liu, S.G.; Chen, C.H.; Wang, D.; Sun, W. The genetic relationship between MVT Pb-Zn deposits and paleo-oil/gas reservoirs at Heba, Southeastern Sichuan Basin. *Earth Sci. Front.* **2013**, *20*, 107–116.
17. Yuan, B.; Mao, J.W.; Yan, X.H.; Wu, Y.; Zhang, F.; Zhao, L.L. Sources of metallogenic materials and metallogenic mechanism of Daliangzi Ore Field in Sichuan Province: Constraints from geochemistry of S, C, H, O, Sr isotope and trace element in sphalerite. *Acta Petrol. Sin.* **2014**, *30*, 209–220.
18. Sun, H.R.; Zhou, J.X.; Huang, Z.L.; Fan, H.F.; Ye, L.; Luo, K.; Gao, J.G. The genetic relationship between Cu-And Zn-dominant mineralization in the tianbaoshan deposit, southwest China. *Acta Petrol. Sin.* **2016**, *32*, 3407–3417.
19. Li, J.H.; Zhang, Y.Q.; Dong, S.W.; Johnston, S.T. Cretaceous tectonic evolution of South China: A preliminary synthesis. *Earth-Sci. Rev.* **2014**, *134*, 98–136. [[CrossRef](#)]
20. Zhao, G.C.; Guo, J.H. Precambrian geology of China: Preface. *Precambrian Res.* **2012**, *222*, 1–12. [[CrossRef](#)]
21. Cui, X.Z.; Wang, J.; Ren, G.M.; Deng, Q.; Sun, Z.M.; Ren, F.; Chen, F.L. Paleoproterozoic tectonic evolution of the Yangtze Block: New evidence from ca. 2.36 to 2.22 Ga magmatism and 1.96 Ga metamorphism in the Cuoque complex, SW China. *Precambrian Res.* **2020**, *337*, 105525. [[CrossRef](#)]
22. Wang, Z.J.; Wang, J.; Du, Q.D.; Deng, Q.; Yang, F. The evolution of the Central Yangtze Block during early Neoproterozoic time: Evidence from geochronology and geochemistry. *J. Asian Earth Sci.* **2013**, *77*, 31–44. [[CrossRef](#)]
23. Zhou, C.M.; Guan, C.G.; Cui, H.; Ouyang, Q.; Wang, W. Methane-derived authigenic carbonate from the lower Doushantuo Formation of South China: Implications for seawater sulfate concentration and global carbon cycle in the early Ediacaran ocean. *Palaeogeogr. Palaeoclimatol. Palaeoecol.* **2016**, *461*, 145–155. [[CrossRef](#)]
24. Condon, D.; Zhu, M.Y.; Bowring, S.; Wang, W.; Yang, A.H.; Jin, Y.G. U-Pb ages from the neoproterozoic Doushantuo Formation, China. *Science* **2005**, *308*, 95–98. [[CrossRef](#)] [[PubMed](#)]
25. Wang, Z.C.; Jiang, H.; Chen, Z.Y.; Liu, J.J.; Ma, K.; Li, W.Z.; Xie, W.R.; Jiang, Q.C.; Zhai, X.F.; Shi, S.Y.; et al. Tectonic paleogeography of Late Sinian and its significances for petroleum exploration in the middle-upper Yangtze region, South China. *Pet. Explor. Dev.* **2020**, *47*, 884–897. [[CrossRef](#)]

26. Liu, S.G.; Li, Z.Q.; Deng, B.; Sun, W.; Li, Z.W.; Ding, Y.; Song, J.M.; Wu, J. Occurrence morphology of bitumen in Dengying Formation deep and ultra-deep carbonate reservoirs of the Sichuan Basin and its indicating significance to oil and gas reservoirs. *Nat. Gas Ind.* **2021**, *41*, 102–112. [[CrossRef](#)]
27. Yang, W.; Wei, G.Q.; Xie, W.R.; Jin, H.; Zeng, F.Y.; Su, N.; Sun, A.; Ma, S.Y.; Shen, J.H.; Wu, S.J. Hydrocarbon accumulation and exploration prospect of mound-shoal complexes on the platform margin of the fourth member of Sinian Dengying Formation in the east of Mianzhu-Changning intracratonic rift, Sichuan Basin, SW China. *Pet. Explor. Dev.* **2020**, *47*, 1262–1274. [[CrossRef](#)]
28. He, D.F.; Li, D.S.; Tong, X.G.; Wu, X.Z. Integrated 3D hydrocarbon exploration in sedimentary basins of China. *Oil Gas Geol.* **2021**, *42*, 265–284.
29. Tan, L.; Liu, H.; Chen, K.; Ni, H.L.; Zhou, G.; Zhang, X.; Yan, W.; Zhong, Y.; Lyu, W.Z.; Tan, X.C.; et al. Sequence sedimentary evolution and reservoir distribution in the third and fourth members of Sinian Dengying Formation, Gaomo area, Sichuan Basin, SW China. *Pet. Explor. Dev.* **2022**, *49*, 871–883. [[CrossRef](#)]
30. Li, Y.; Wang, X.Z.; Feng, M.Y.; Zeng, D.M.; Xie, S.Y.; Fan, R.; Wang, L.J.; Zeng, T.; Yang, X.F. Reservoir characteristics and genetic differences between the second and fourth members of Sinian Dengying Formation in northern Sichuan Basin and its surrounding areas. *Pet. Explor. Dev.* **2019**, *46*, 54–66. [[CrossRef](#)]
31. Zhou, H.; Li, W.; Zhang, B.M.; Liu, J.J.; Deng, S.H.; Zhang, S.B.; Shan, X.Q.; Zhang, J.; Wang, X.B.; Jiang, H. Formation and evolution of Upper Sinian to Lower Cambrian intraplatformal basin in Sichuan Basin. *Acta Pet. Sin.* **2015**, *36*, 310–323. [[CrossRef](#)]
32. Zhou, Y.; Yang, F.L.; Ji, Y.L.; Zhou, X.F.; Zhang, C.H. Characteristics and controlling factors of dolomite karst reservoirs of the Sinian Dengying Formation, central Sichuan Basin, southwestern China. *Precambrian Res.* **2020**, *343*, 105708. [[CrossRef](#)]
33. Gu, Z.D.; Zhang, W.; Yuan, M. Zircon SHRIMP U-Pb dating of basal granite and its geological significance in Weiyuan area of Sichuan Basin. *Sci. Geol. Sin.* **2014**, *49*, 202–213.
34. Fan, H.D. Tectonic Evolution and Formation Mechanism of Paleo-Uplift in the Northeastern Sichuan Basin. Master's Thesis, China University of Geosciences, Beijing, China, 2018.
35. Chen, J.T.; Lee, J.H. Current Progress on the Geological Record of Microbialites and Microbial Carbonates. *Acta Geol. Sin. (Chin. Ed.)* **2014**, *88*, 260–275. [[CrossRef](#)]
36. Wen, L.; Wang, W.Z.; Zhang, J.; Luo, B. Classification of Sinian Dengying Formation and sedimentary evolution mechanism of Gaoshiti-Moxi area in central Sichuan Basin. *Acta Petrol. Sin.* **2017**, *33*, 1285–1294.
37. Peng, J.; Zhang, H.B.; Lin, X.X. Study on characteristics and genesis of botryoidal dolostone of the Upper Sinian Dengying Formation: A case study from Hanyuan region, Sichuan, China. *Carbonate. Evaporite.* **2018**, *33*, 285–299. [[CrossRef](#)]
38. Zhao, W.Z.; Wang, Z.C.; Jiang, H.; Fu, X.D.; Xie, W.R.; Xu, A.N.; Shen, A.J.; Shi, S.Y.; Huang, S.P.; Jiang, Q.C. Exploration status of the deep Sinian strata in the Sichuan Basin: Formation conditions of old giant carbonate oil/gas fields. *Nat. Gas Ind.* **2020**, *40*, 1–10. [[CrossRef](#)]
39. Xu, C.C.; Shen, P.; Yang, Y.M.; Zhao, L.Z.; Luo, B.; Wen, L.; Chen, K.; Ran, Q.; Zhong, Y.; Peng, H.L. New understandings and potential of Sinian-Lower Paleozoic natural gas exploration in the central Sichuan paleo-uplift of the Sichuan Basin. *Nat. Gas Ind.* **2020**, *40*, 1–9. [[CrossRef](#)]
40. Sun, W.D.; McDonough, W. Chemical and isotopic systematics of oceanic basalts: Implications for mantle composition and processes. *Geol. Soc.* **1989**, *42*, 313–345. [[CrossRef](#)]
41. Roberts, N.M.W.; Drost, K.; Horstwood, M.S.A.; Condon, D.J.; Chew, D.; Drake, H.; Milodowski, A.E.; McLean, N.M.; Smye, A.J.; Walker, R.J.; et al. Laser ablation inductively coupled plasma mass spectrometry (LA-ICP-MS) U-Pb carbonate geochronology: Strategies, progress, and limitations. *GChron* **2020**, *2*, 33–61. [[CrossRef](#)]
42. Lan, Z.W.; Roberts, N.M.W.; Zhou, Y.; Zhang, S.J.; Li, Z.S.; Zhao, T.P. Application of in situ U-Pb carbonate geochronology to Stenian-Tonian successions of North China. *Precambrian Res.* **2022**, *370*, 106551. [[CrossRef](#)]
43. Xiong, S.F.; Jiang, S.Y.; Zhao, J.X.; Niu, P.P.; Ma, Y.; Bai, X.Y. Dating Precambrian sedimentary carbonate strata by in situ U-Pb isotopes of dolomite. *Precambrian Res.* **2023**, *393*, 107088. [[CrossRef](#)]
44. Shen, A.J.; Hu, A.P.; Cheng, T.; Liang, F.; Pan, W.Q.; Feng, Y.X.; Zhao, J.X. Laser ablation in situ U-Pb dating and its application to diagenesis-porosity evolution of carbonate reservoirs. *Pet. Explor. Dev.* **2019**, *46*, 1062–1074. [[CrossRef](#)]
45. Wang, W.; Zhou, M.Z.; Chu, Z.Y.; Xu, J.J.; Li, C.F.; Luo, T.Y.; Guo, J.H. Constraints on the Ediacaran-Cambrian boundary in deep-water realm in South China: Evidence from zircon CA-ID-TIMS U-Pb ages from the topmost Liuchapo Formation. *Sci. China Earth Sci.* **2020**, *63*, 1176–1187. [[CrossRef](#)]
46. Jiang, L.; Shen, A.J.; Wang, Z.C.; Hu, A.P.; Wang, Y.S.; Luo, X.Y.; Liang, F.; Azmy, K.; Pan, L.Y. U-Pb geochronology and clumped isotope thermometry study of Neoproterozoic dolomites from China. *Sedimentology* **2022**, *69*, 2925–2945. [[CrossRef](#)]
47. Lottermoser, B.G. Rare earth elements and hydrothermal ore formation processes. *Ore Geol. Rev.* **1992**, *7*, 25. [[CrossRef](#)]
48. Shi, Z.J.; Liang, P.; Wang, Y.; Hu, X.Q.; Tian, Y.M.; Wang, C.C. Geochemical characteristics and genesis of grapestone in Sinian Dengying Formation in south-eastern Sichuan basin. *Acta Petrol. Sin.* **2011**, *27*, 2263–2271.
49. Shi, Z.J.; Wang, Y.; Tian, Y.M.; Wang, C.C. Cementation and diagenetic fluid of algal dolomites in the Sinian Dengying Formation in southeastern Sichuan Basin. *Sci. China Earth Sci.* **2013**, *56*, 192–202. [[CrossRef](#)]
50. Qian, Y.X.; Feng, J.F.; He, Z.L.; Zhang, K.Y.; Jin, T.; Dong, S.F.; You, D.H.; Zhang, Y.D. Applications of petrography and isotope analysis of micro-drill samples to the study of genesis of grape-like dolomite of the Dengying Formation in the Sichuan Basin. *Oil Gas Geol.* **2017**, *38*, 665–676. [[CrossRef](#)]

51. Xu, Z.H.; Lan, C.J.; Zhang, B.J.; Hao, F.; Lu, C.J.; Tian, X.W.; Zou, H.Y. Impact of diagenesis on the microbial reservoirs of the terminal Ediacaran Dengying Formation from the Central to Northern Sichuan Basin, SW China. *Mar. Pet. Geol.* **2022**, *146*, 105924. [[CrossRef](#)]
52. Liu, W.H.; Zhang, X.J.; Zhang, J.; Jiang, M.R. Sphalerite Rb-Sr Dating and in situ Sulfur Isotope Analysis of the Daliangzi Lead-Zinc Deposit in Sichuan Province, SW China. *J. Earth Sci.* **2018**, *29*, 573–586. [[CrossRef](#)]
53. Zhou, Z.B.; Wen, H.J.; Qin, C.J.; de Fourestier, J.; Liu, L.; Shi, Q.P. The genesis of the Dahebian Zn-Pb deposit and associated barite mineralization: Implications for hydrothermal fluid venting events along the Nanhua Basin, South China. *Ore Geol. Rev.* **2018**, *101*, 785–802. [[CrossRef](#)]
54. He, Z.W.; Li, Z.Q.; Li, B.; Chen, J.; Xiang, Z.P.; Wang, X.F.; Du, L.J.; Huang, Z.L. Ore genesis of the Yadu carbonate-hosted Pb-Zn deposit in Southwest China: Evidence from rare earth elements and C, O, S, Pb, and Zn isotopes. *Ore Geol. Rev.* **2021**, *131*, 104039. [[CrossRef](#)]
55. Yang, H.Y.; Xiao, J.F.; Xia, Y.; Xie, Z.J.; Tan, Q.P.; Xu, J.B.; Guo, H.Y.; He, S.; Wu, S.W. Origin of the Ediacaran Weng'an and Kaiyang phosphorite deposits in the Nanhua basin, SW China. *J. Asian Earth Sci.* **2019**, *182*, 103931. [[CrossRef](#)]
56. Zhang, F.; Fan, H.F.; Liu, X.Q.; Zhang, H.J.; Wen, H.J.; Tang, Y.; Shang, P.Q. Distinct REY sources recorded in the Doushantuo phosphorite. *Ore Geol. Rev.* **2023**, *157*, 105470. [[CrossRef](#)]
57. Wang, T.; Li, Z.W.; Chen, H.D.; Hou, M.C. Differential uplift process in mesozoic-cenozoic Longmen mountains along eastern margin of Tibetan Plateau. *J. Chem. Pharm. Res.* **2014**, *6*, 494–501.
58. Deng, J.; Wang, Q.F.; Chen, F.C.; Li, G.J.; Yang, L.Q.; Wang, C.M.; Zhang, J.; Sun, X.; Shu, Q.H.; He, W.Y.; et al. Further discussion on the Sanjiang Tethyan composite metallogenic system. *Earth Sci. Front.* **2020**, *27*, 106–136. [[CrossRef](#)]
59. Lu, G.; Li, C.X.; Li, W.Z.; Deng, S.; Zhang, J.Y. Structural Geometry and Kinematics of Thrust Belts between the Dabashan and Eastern Sichuan Basin, South China Block: Constraints from (U-Th)/He Dating and Seismic Data. *Geol. Soc. Am. Bull.* **2021**, *133*, 1749–1764. [[CrossRef](#)]
60. Mo, X.X.; Zhao, Z.D.; Deng, J.F.; Flower, M.; Yu, X.H.; Luo, Z.H.; Li, Y.G.; Zhou, S.; Dong, G.C.; Zhu, D.C.; et al. Petrology and geochemistry of postcollisional volcanic rocks from the Tibetan plateau: Implications for lithosphere heterogeneity and collision-induced asthenospheric mantle flow. *Geol. Soc. Am. Bull.* **2006**, *409*, 507–530. [[CrossRef](#)]
61. Zou, C.N.; Zhao, W.Z.; Jia, C.Z.; Zhu, R.K.; Zhang, G.Y.; Zhao, X.F.; Yuan, X.J. Formation and distribution of volcanic hydrocarbon reservoirs in sedimentary basins of China. *Pet. Explor. Dev.* **2008**, *35*, 257–271. [[CrossRef](#)]
62. Deng, J.; Wang, C.M.; Li, G.J. Style and process of the superimposed mineralization in the Sanjiang Tethys. *Acta Petrol. Sin.* **2012**, *28*, 1349–1361.
63. Mao, J.W.; Xie, G.Q.; Zhang, Z.H.; Li, X.F.; Wang, Y.T.; Zhang, C.Q.; Li, Y.F. Mesozoic large-scale metallogenic pulses in North China and Corresponding geodynamic setting. *Acta Petrol. Sin.* **2005**, *21*, 169–188.
64. Dang, L.R.; Zheng, R.C.; Zheng, C.; Wen, Q.B.; Chen, S.C.; Liao, J. Origins and diagenetic system of dolomite reservoirs in the Upper Permian Changxing Fm, eastern Sichuan Basin. *Nat. Gas Ind.* **2011**, *31*, 47–52. [[CrossRef](#)]
65. Zheng, R.C.; Dang, L.R.; Wen, H.G.; Chen, Z.W.; Chen, F.M.; Zhang, H.J. Diagenesis characteristics and system for dolostone in Feixianguan formation of Northeast Sichuan. *Earth Sci.—J. China Univ. Geosci.* **2011**, *36*, 659–669.
66. Sun, W.; Liu, S.G.; Cao, J.X.; Deng, B.; Song, J.M.; Wang, G.Z.; Yuan, Y.; Wang, H. Analysis on the formation conditions of large-scale marine deep and super-deep strata gas fields in the middle-northern segments of western Sichuan Superimposed Basin, China. *Acta Petrol. Sin.* **2017**, *33*, 1171–1188.
67. Zhou, J.X.; Huang, Z.L.; Bao, G.P. Geological and sulfur-lead-strontium isotopic studies of the Shaojiwan Pb-Zn deposit, southwest China: Implications for the origin of hydrothermal fluids. *J. Geochem. Explor.* **2013**, *128*, 51–61. [[CrossRef](#)]
68. Li, W.C.; Liu, X.L. The metallogenic regularity related to the tectonic and petrographic features of Pulang porphyry copper orefield, Yunnan, and its ore-controlling characteristics. *Earth Sci. Front.* **2015**, *22*, 53–66. [[CrossRef](#)]
69. Ren, J.S.; Zhao, L.L.; Xu, Q.Q.; Zhu, J.B. Global tectonic position and geodynamic system of China. *Acta Geol. Sin. (Chin. Ed.)* **2016**, *90*, 2100–2108.
70. Hu, J.; Qiu, J.S.; Xu, X.S.; Wang, X.L.; Li, Z. Geochronology and geochemistry of gneissic metagranites in eastern Dabie Mountains: Implications for the Neoproterozoic tectono-magmatism along the northeastern margin of the Yangtze Block. *Sci. China Earth Sci.* **2010**, *53*, 501–517. [[CrossRef](#)]
71. Pan, G.T.; Lu, S.N.; Xiao, Q.H.; Zhang, K.X.; Yin, F.G.; Hao, G.J.; Luo, M.S.; Ren, F.; Yuan, S.H. Division of tectonic stages and tectonic evolution in China. *Earth Sci. Front.* **2016**, *23*, 1–23. [[CrossRef](#)]
72. Pan, G.T.; Xiao, Q.H.; Lu, S.N.; Deng, J.F.; Feng, Y.M.; Zhang, K.X.; Zhang, Z.Y.; Wang, F.G.; Xing, G.F.; Hao, G.J.; et al. Subdivision of tectonic units in China. *Geol. China* **2009**, *36*, 1–28.
73. Zhao, X.F.; Zhou, M.F.; Li, J.W.; Sun, M.; Gao, J.F.; Sun, W.H.; Yang, J.H. Late Paleoproterozoic to early Mesoproterozoic Dongchuan Group in Yunnan, SW China: Implications for tectonic evolution of the Yangtze Block. *Precambrian Res.* **2010**, *182*, 57–69. [[CrossRef](#)]

74. Wang, L.J.; Yu, J.H.; Griffin, W.L.; O'Reilly, S.Y. Early crustal evolution in the western Yangtze Block: Evidence from U-Pb and Lu-Hf isotopes on detrital zircons from sedimentary rocks. *Precambrian Res.* **2012**, *222*, 368–385. [[CrossRef](#)]
75. Xing, F.C.; Hou, M.C.; Lin, L.B.; Xu, S.L.; Hu, H.R. The records and its dynamic genesis discussion of tectonic movement during the Late Sinian and the Early Cambrian of Sichuan Basin. *Earth Sci. Front.* **2015**, *22*, 115–125. [[CrossRef](#)]

**Disclaimer/Publisher's Note:** The statements, opinions and data contained in all publications are solely those of the individual author(s) and contributor(s) and not of MDPI and/or the editor(s). MDPI and/or the editor(s) disclaim responsibility for any injury to people or property resulting from any ideas, methods, instructions or products referred to in the content.